HHS Public Access

Author manuscript

Nat Struct Mol Biol. Author manuscript; available in PMC 2017 October 03.

Published in final edited form as:

Nat Struct Mol Biol. 2017 March ; 24(3): 248–257. doi:10.1038/nsmb.3369.

Eukaryotic Rad50 Functions as A Rod-shaped Dimer

Young Bong Park[1,5], **Marcel Hohl**[2,5], **Michał Padjasek**[3], **Eunyoung Jeong**[1], **Kyeong Sik Jin**[4], **Artur Krężel**[3], **John H. J. Petrini**[2], and **Yunje Cho**[1]

[1]Department of Life Sciences, Pohang University of Science and Technology, Pohang, South Korea [2]Molecular Biology Program, Memorial Sloan-Kettering Cancer Center, New York, NY 10021, USA [3]Laboratory of Chemical Biology, University of Wrocław, Joliot-Curie 14a, 50-383 Wrocław, Poland [4]Pohang Accelerator Laboratory, Pohang University of Science and Technology, Pohang, South Korea

Abstract

The Rad50 hook interface is crucial for assembly and functions of the Mre11 complex. Previous analyses suggest that Rad50 molecules interact within (intra-complex) or between (inter-complex) dimeric complexes. In this study, we determined the structure of the human Rad50 hook and coiled-coil domain. The data suggest that the predominant structure is the intra-complex, in which the two parallel coiled-coils proximal to the hook form a rod-shape, and that a novel interface within the coiled-coil domains of Rad50 stabilizes the interaction of Rad50 protomers within the dimeric assembly. In yeast, removal of the coiled-coil interface compromised Tel1 activation without affecting DNA repair, while simultaneous disruption of that interface and the hook phenocopied a null mutation. The results demonstrate that the hook and coiled-coil interfaces coordinately promote intra-complex assembly and define it as the functional form of the Mre11 complex.

The Mre11 complex (Mre11-Rad50-Nbs1/Xrs2) plays a central role in the eukaryotic DNA damage response (DDR) in which it is a sensor of DNA double strand breaks (DSBs), and thereby governs DNA damage signaling as well as DSB repair. This elongated-shaped complex appears to contain two major dimerization interfaces that link the trimeric assemblies of Mre11, Rad50 and Nbs1/Xrs2[1–4]. One is within the globular domain via Rad50 and Mre11. The second, called the zinc-hook, is distal to the globular domain

Correspondence should be addressed to yunje@postech.ac.kr or petrinij@mskcc.org.
[5]These authors equally contributed to this work

Accession codes

Coordinates and structure factors have been deposited in the Protein Data Bank under accession codes PDB 5GOX.
Source data for figure 4j, 5d and 6 are available with the paper online. Also, other source data are available upon request.

Author contributions

Y.P. carried out crystallization and structure determination; Y.P., M.P., M.H., and E.J. participated in biochemical experiments. K. J. performed SAXS analyses. M.H. and J.H.J.P. designed and performed yeast genetics experiment. Y.C. and J.H.J.P. designed research in consultation with A.K. J.H.J.P., Y.C., A.K. and M.H. wrote the manuscript.

Competing financial interests

The authors declare no competing financial interest.

separated by the long antiparallel coiled-coil domains of Rad50 and is a site of homotypic Zn^{2+}-dependent dimerization.

The enzymatic and DNA binding functions of the Mre11 complex are specified within the globular domain, which is likely to govern DNA damage signaling as well[5–8]. In the ATP-bound configuration, the Mre11 nuclease domains are occluded by Rad50[9,10], and DNA binds at the central groove between the Rad50 dimers in ATP-dependent manner, although additional DNA binding modes are suggested[6, 11–14]. This closed form of the complex appears to be required for DNA dependent ATM activation[15]. ATP hydrolysis induces a profound conformational change in the Rad50 dimer, which opens the globular domain, and renders the Mre11 nuclease domain accessible to the DNA substrate[6–10,16–18].

Dimerization at the zinc-hook domain is also critical for Mre11 complex functions and the coiled-coils appears to transmit structural information between the two domains[19–23]. In the *Pyrococcus furiosus* Rad50 (*Pf*Rad50) hook domain, Zn^{2+} coordination dictates that the hook-proximal coiled-coils from each Rad50 protomer point in opposite directions toward their respective globular domains at 140 degrees angle relative to each other[21]. That structural information as well as genetic data regarding the roles of the complex in DSB repair led to a model wherein hook-mediated dimerization between Mre11 complex dimeric assemblies would bridge DNA molecules such as sister chromatids *in trans*[8] (Fig. 1a). That arrangement is referred to here as the “inter-complex”, and was suggested to account for the promotion of homologous recombination between sister chromatids (SCR) by the Mre11 complex, with the complexes associated *in trans* each envisaged to engage a sister chromatid[21–26]. This model is also consistent with atomic force microscopy (AFM) showing that DNA binding induced a parallel arrangement of the coiled-coil arms, suggestive of “reaching out” to promote engagement of apical hook domains *in trans*[27].

An alternative structural model suggests that the MRN complex functions in a ring-like structure in which dimerization at the hook and globular domain completes the dimeric assembly (Fig. 1a). In this conception, which is referred to herein as the “intra-complex”, hook-dimerization promotes interaction of the Rad50 ATPase domains[5,6,15].

This idea resonates with mounting evidence that hook-mediated dimerization is essential for the functions of the globular domain. Deletion of the hook domain or alteration of the invariant cysteines phenocopies *rad50Δ*. Mutations of the conserved residues between the invariant cysteines (*rad50-46*, *-47*, and *-48*) impair Zn^{2+} coordination, NHEJ, and DNA end resection. Those phenotypes can be suppressed by intragenic mutations in the coiled-coils, supporting the interpretation that the coiled-coils integrate structural information of the hook and globular domains[21,22,25].

With respect to the inter- vs. intra-complex, it is notable that the *rad50-46*, *-47*, and *-48* mutations do not impair SCR, despite each exhibiting marked deficits in Zn^{2+} binding[20]. That observation undermines the fundamental premise of the inter-complex model as it posits that Zn^{2+}-mediated dimerization is required for bridging sister chromatids and thereby promoting SCR[8,21]. Moreover, the *rad50-46*, *-47*, and *-48* mutations each strongly compromise ATM/Tel1 activation, implicating the apex of Rad50 in the activation of DNA

damage signaling. To resolve this paradox, we performed structural, biochemical, biophysical and genetic analyses of the human and yeast Rad50 hook domain and provide insight regarding conserved (*e.g.*, DNA repair) as well as eukaryal (*e.g.*, ATM activation) Mre11 complex function in the DNA damage response.

RESULTS

The structure of the human Rad50 hook domain reveals a novel coiled-coils interface

We determined the crystal structure of "*Hs*Rad50HCC182" (182 residues from 585 to 766 for hook and coiled-coil domains) of human Rad50 at 2.4 Å resolution (Fig. 1a,b, Supplementary Fig.1a,b). A Rad50HCC182 dimer forms a rod-shaped structure, in which the two hook motifs (residues 674–690) from Rad50A and Rad50B molecules coordinate a Zn^{2+} at the apex and the parallel coiled-coils originating from the hook tightly packed side by side and extended away (Fig. 1c, d). In addition to the hook-mediated dimerization interface, the structure revealed a dimerization interface within the coiled-coil domains, which likely cooperates with the hook domain interface to stabilize the intra-complex configuration as the primary functional form of the Mre11 complex.

Each Rad50HCC182 monomer consists of five helices, in which two helices (H1 and H2) are packed against three helices (H3 to H5) to form an antiparallel coiled-coil (Fig. 1b, c, Supplementary Fig. 1c). The Rad50HCC182 dimer can be divided into three layers starting at the apex and continuing downward to the distal end (Fig. 1c, d, Fig. 2a–c). On top, the hook motif of Rad50A makes head-to-head interactions with opposite hook motif and with the helices H2 and H3 (hereafter "Connecting Helices") from Rad50B (Fig. 2a, b). Each hook motif from Rad50 dimer coordinates a Zn^{2+} ion *via* Cys681 and Cys684. In addition, the hook-interface is further stabilized by an ion pair (Arg686 and Glu693), a hydrogen-bond (Arg686 and Val687) and extensive hydrophobic interactions (Fig. 2a, b). Although the hook-interface is a conserved feature of the Mre11 complex, this dimerization interface is the most remarkable departure from the *Pf*Rad50 hook domain in which the equivalent coiled-coils point in opposite directions, forming a wide-open structure (Fig. 2b, d, e). Most of the residues in the hook-mediated interface are highly conserved throughout eukaryotic species (Supplementary Fig. 1c, d).

The second layer is defined by a novel interface formed by coiled-coils dimerization (Fig. 2b, c). This interface covers about 910 $Å^2$, comparable to the area of the hook interface (907 $Å^2$). Hydrophobic interactions between helices H2 and H2' on top and between helices H4 and H4' at the bottom stabilize this interface. By contrast, middle region of the interface contains a number of charged residues that contribute to ion-pair networks. Although the residues at this interface are only partially conserved in eukaryotic Rad50 molecules, the interface is likely to be formed in all eukaryotes (Supplementary Fig. 1c, e).

The hinge loop promotes mobility of the downstream coiled-coils

The third layer is formed by helices H1, H4 and H5 and is separated from the coiled-coil interface by a highly flexible five-residue "hinge" loop (CGSQD) which is likely to permit mobility of the third layer and downstream coiled-coils (Fig. 1c). Indeed, the coiled-coils in

the third layer make no inter-molecular contact and are separated by 20 Å. Further, whereas the first and second layers of Rad50A can be aligned to Rad50B molecule with a r.m.s.d. value of 1.6 Å for Cα atoms, the superposition of the third layer of the coiled-coils in that alignment deviates more than 40 Å (Fig. 2f). In light of the stable interactions within the hook domain and the coiled-coil interface in the intra-complex form, the hinge loop is likely required to accommodate the ATP hydrolysis dependent structural transitions noted previously[6,9,16].

The importance of the flexibility of the hinge loop was demonstrated by replacement of the three residues near and at the loop by proline in budding yeast *rad50* (E639P, C641P, D644P, *rad50-PPP* mutant) to constrain flexibility of this region (Supplementary Fig. 2a). *rad50-PPP* alone did not confer sensitivity to methyl methanesulfonate (MMS) or camptothecin (CPT) induced damage. We combined this mutation with *rad50-48*, which destabilizes the hook interface, but is similarly resistant to MMS and CPT[20]. *rad50-PPP rad50-48* (*rad50-PPP-48)* double mutants exhibited severe sensitivity and severely impaired Mre11 complex integrity (Supplementary Fig. 2b–e). These data indicate that the hook domain and hinge loop cooperate to influence the downstream coiled-coils and globular domain.

Solution structure of the human Rad50 coiled-coils at the apex

The intra-complex suggested by the crystal structure was validated by in solution approaches. First, we performed small angle X-ray scattering (SAXS) analysis of the *Hs*Rad50HCC construct that contains the two interfaces (residues 635 to 730, Fig. 3a–c). The structural parameters obtained from a SAXS analysis corresponded to those of the rod-shaped model of human Rad50HCC (Supplementary Table 1, Supplementary Note 1). In contrast, SAXS analysis of *Pf*Rad50 hook coiled-coil (residues 351 to 532) equivalent to the hRad50HCC exhibited a wide-open structure, consistent with the reported crystal structure[21] (Supplementary Fig. 3a–c).

We propose that the coiled-coil and Zn^{2+}-hook interfaces cooperate to stabilize the rod-shaped intra-complex of human Rad50. Two lines of evidence support this interpretation. First, ultracentrifugation analyses revealed coiled-coil interface-dependent dimerization of Rad50HCC in the absence of Zn^{2+} (Supplementary Fig. 1a), suggesting that dimerization of the Rad50HCC182 protein in the Zn^{2+}-free solution occurs via the coiled-coils interface. Second, FRET analyses with a 72 residue-peptide (651 to 722) lacking the coiled-coil interface revealed a Zn^{2+} dependent alignment of the coiled coils. Equimolar mixtures of differently labeled proteins (DNS and FAM, or FAM and TAMRA as donor and acceptor) were used for FRET analyses, which were assessed over a range of free Zn^{2+} concentrations[28] (Fig. 4a–g, Supplementary Table 2). A strong Zn^{2+}-dependent FRET signal indicates that the coiled-coil ends from each monomer are ~30 Å apart in the presence of zinc, consistent with the crystal structure (Fig. 4b, d, Supplementary Table 3).

To further validate and probe the landscape of the coiled-coil interface, we undertook chemical crosslinking experiment using variants of the *Hs*Rad50HCC182 fragment (Fig. 4h–m) in which residues of the interface without or with concomitant substitutions of the hook domain. We first observed that H_2O_2 treatment failed to induce crosslinking of the hook domain cysteines. The inaccessibility of those residues is consistent with the crystal

structure (Fig. 2a, 4h). Next, we introduced cysteine residues at the position of Lys599 in helix H1 or Ser738 in helix H4 in the combination with a wild type hook domain. The distance between two modeled Cys599 or Cys738 residues in Rad50 dimer was 13.7 Å and 7.2 Å, respectively (Fig. 4i). The two protomers of K599C or S738C *Hs*Rad50HCC182 dimer are crosslinked by bis-(maleimido) hexane (BMH, optimal crosslink distance 13 Å) and bis-(maleimido) ethane (BMOE, 8 Å), supporting the crystal structure (Fig. 4j).

Generation of human Rad50 “hook” and “coiled-coils” mutants

Our analysis of human Rad50 suggests that the predominant structure is the rod-shaped intra-complex, and we hypothesize that stabilization of this arrangement is effected coordinately by the hook domain and coiled-coil interface. To test this hypothesis we combined alterations in the hook domain with the coiled-coil mutations described above and examined their effects on crosslinking.

The human Rad50 hook domain was replaced by the hinge domain of the *Thermotoga maritima* Structural Maintenance of Chromosome (SMC) protein (1GXL)[29] or by the *P. furiosus* Rad50 hook domain (*Pf*hook; Supplementary Table 4, Supplementary Fig. 3d–g). Crosslinking analysis revealed that neither the K599C nor S738C mutants can be crosslinked by BMH or BMOE, indicating that that SMC hinge or *Pf*hook alter the path of the coiled-coils and increased the distance between the protomers in those mutants (Fig. 4k, i). This interpretation was confirmed by FRET analysis that clearly showed an absence of energy transfer between two N-termini of protomers in a dimer (Fig. 4e, Supplementary Fig. 3d–f).

To directly assess the functional interactions of the coiled-coil interface and hook domain, we removed the 104 residues comprising the interface to create the ΔCC mutant (Rad50ΔCC) (Supplementary Table 4). The Rad50ΔCC peptide was primarily dimeric in gel filtration analysis (Supplementary Fig. 4a). Although both crosslinking and FRET analysis revealed a decrease in dimerization (Figs 4f, 4m), the emission signal indicates that the ends of the coiled-coils in Rad50ΔCC are relatively close proximity estimated to be around 46 Å (Supplementary Table 3). On this basis, we conclude that the Rad50ΔCC mutant maintains similar rod-shaped intra-complex structure observed in wild-type Rad50HCC182.

We modeled the *S. cerevisiae rad50-48* hook mutation (S685R and Y688R; S679R and P682R in *Hs*Rad50) in Rad50HCC182 (Supplementary Fig. 1d–f). As noted previously, the *rad50-48* mutant exhibited wild type DNA repair, despite a significant deficit in Zn^{2+}-mediated dimerization (Fig. 4m)[20]. We reasoned that combining *rad50-48* with *ΔCC* would disrupt both interfaces at the apex. As expected, the ΔCC-48 K599C mutant exhibited marked reduction in the levels of crosslinked dimers relative to the ΔCC K599C mutant (Fig. 4m). FRET analysis also suggested that ΔCC-48 mutant failed to assemble correctly (Fig. 4g), and circular dichroism analyses revealed that the addition of the *rad50-48* hook mutation altered the conformation of the ΔCC mutant (Supplementary Fig. 4b).

In vivo assessments support the intra-complex model

Collectively, the structural and biochemical analyses support the view that the human Rad50 assumes a rod like intra-complex structure which is coordinately stabilized by the hook domain and the coiled-coil interface. This model accounts for the fact that *rad50-46*, *-47*,

and *-48* mutations which destabilize the hook interface retain the ability to promote SCR; the coiled-coil interface is likely to compensate for the decrement in hook stability[20]. The model thus predicts that concomitant destabilization of the hook domain and coiled-coil interfaces would impair Mre11 complex functions *in vivo*.

We tested that prediction by modeling the SMC hinge or *Pf*hook mutants described above in *S. cerevisiae* (Supplementary Fig. 1c, 3, Supplementary Table 4). Human Rad50 shares 70% of sequence similarity (29% identity) with yeast Rad50. The mutants were integrated into the chromosome and expressed from the native *RAD50* promoter. The SMC hinge or *Pf*hook *rad50* mutants were treated with MMS or CPT, and exhibited pronounced sensitivity both at higher MMS doses (> 100 fold less survival than *WT* at 0.02% MMS), although both mutants were substantially better than *rad50Δ* at lower MMS doses, suggesting that the hook substitutions retain a degree of functionality (Fig. 5a). The same trend was evident upon CPT treatment (Fig. 5b). Given that the hook substitutions are likely to impair the stability of the coiled-coil interface, these data support a functional link between that interface and the hook domain *in vivo*. As predicted by the *in vitro* data as well as previous yeast studies[20,25], neither the *rad50ΔCC* nor *rad50-48* mutant exhibited sensitivity to either MMS or CPT. However, the *rad50ΔCC rad50-48* double mutant (*rad50-ΔCC-48)* was extremely sensitive, approximating the phenotypes observed for SMC hinge and *Pf*hook strains (Fig. 5a, b).

To address the molecular basis for the sensitivities observed, Mre11 complex integrity was assessed via immunoprecipitation with Mre11 and Rad50 antisera. Rad50 protein levels were not overtly altered in any of the mutants. Interactions between Rad50 and Mre11 were largely unaffected except in *rad50-ΔCC-48* double mutants, in which the level of the mutant protein in Mre11 immunoprecipitations was markedly reduced (Fig. 5c). This outcome is reminiscent of previous studies in which mutations in the hook domain phenocopy *rad50Δ* due to disruption of Rad50 interaction with Mre11[20,25].

The Mre11 complex also participates in NHEJ[30–32] and the ATP-bound “closed” form of Rad50 appears to be required for NHEJ activity[5]. We examined NHEJ of an HO break in the hook substitution and coiled-coil interface mutants in a strain lacking a homologous template. Following transient (2 hr) induction of the HO endonuclease, rejoining of the HO site was inferred from the ability of cells to form colonies within three to five days. 46% of *WT* and 2% of *rad50Δ* cells formed colonies in this setting (Fig. 5d). The hook substitution mutants were severely impaired, but exhibited approximately three-fold higher viability than *rad50Δ*. The same was true of the *rad50-ΔCC-48* double mutant. Whereas the single *rad50-48* and *rad50ΔCC* were only marginally (two fold) reduced relative to *WT*, viability of *rad50-ΔCC-48* double mutants was reduced by more than eight fold (Fig. 5d). Collectively, these data suggest that the intra-complex is operative during Mre11 complex-mediated DSB repair by SCR as well as NHEJ.

The intra-complex: meiosis and checkpoint signaling

Next, we examined two other Mre11 complex-dependent functions, meiotic recombination[33] and checkpoint signaling. Diploid strains expressing Rad50 hook substitution or coiled-coil interface mutant proteins were induced to sporulate and the frequency of viable spore formation was assessed. The trends observed for DSB repair functions were recapitulated in

this setting. The spore viability and sporulation efficiency of *rad50ΔCC* and *rad50-48* were reduced approximately two fold relative to wild type, whereas the hinge (4 and 2%, respectively), *Pf*hook mutant (3 and 9%), and *rad50ΔCC-48* mutant phenocopied *rad50Δ* in this setting (Fig. 6a).

We next examined two indices of ATM/Tel1 activation, which appears to depend on the ATP-bound MRN/X form of the complex[15,34–36], telomere length and Rad53 activation. Telomere length in the hook substitution and coiled-coil interface mutants was assessed by Southern blotting (Supplementary Fig. 5a). Telomere shortening was observed in all cases, suggesting that Tel1 signaling was defective in all mutants.

To assess Tel1 and Rad53 activation, we examined the survival of Rad50 mutants deficient for both Mec1 and Sae2 (*mec1Δ sae2Δ* double mutants). Mec1 deficiency is suppressed in *sae2Δ* cells via activation of a Tel1- and Mre11- dependent pathway (the TM pathway)[34]. Rad53 activation, as inferred from the appearance of a slower migrating phosphorylated form was also assessed by Western blot.

In Rad50 proficient cells, MMS sensitivity and Rad53 phosphorylation deficits were restored by Sae2 deficiency, whereas that suppression was markedly impaired in the hook substitution mutants (Fig. 6b). As with DSB repair and meiosis, *rad50-48 mec1Δ* and *rad50ΔCC mec1Δ* approximated wild type *RAD50 mec1Δ* survival after MMS treatment, but the *rad50ΔCC-48 mec1Δ* mutant phenocopied the *rad50Δ mec1Δ* control (Fig. 6a,b). Nevertheless, in *mec1Δ sae2Δ* cells, neither *rad50-48* nor *rad50ΔCC* single mutants showed increased MMS survival in comparison to the survival in *mec1Δ* cells (Fig. 6b), and the levels of DNA damage induced Rad53 phosphorylation in *mec1Δ sae2Δ* cells were markedly reduced in all mutants (Fig. 6c). These observations indicate that *rad50ΔCC*, as previously shown for *rad50-48*[20] represents a separation of function mutant in which DNA repair is intact (as indicated by growth on MMS plates) and DNA damage signaling is impaired (as indicated by the decrement in Rad53 phosphorylation).

Because Tel1/ATM activation depends on the ATP-bound Mre11-Rad50-Nbs1/Xrs2-DNA complex[15], we measured ATP binding and hydrolysis properties of human Mre11 complexes containing various Rad50 mutants. All mutants exhibited 7 to 15-fold decreased ATP-hydrolysis (Fig. 6d) while maintaining similar ATP binding activities (Fig. 6e) compared to that of the wild type Rad50. DNA-binding activities were significantly decreased in the ΔCC-48 and *Pf*hook mutant complexes, whereas ΔCC exhibited essentially wild type DNA binding activity (Fig. 6f, Supplementary Fig. 5b–e). These results clearly indicate that structural alterations of the globular domain via conformational changes at the apex and coiled-coils affected Tel1 activation. These data offer compelling support that the intra-complex is stabilized by the coordinate actions of the hook and coiled-coil interface and that the intra-complex is operative in DNA damage signaling as well as DNA repair.

Discussion

The goal of this study was to determine the spatial arrangement of human Mre11 complex components within the dimeric assembly that could account for the diverse phenotypic

outcomes observed in hook domain mutants. The available data suggest two models for Mre11 complex assembly: the inter-complex and the intra-complex (Fig. 1a).

Structural, in solution, and *in vivo* analyses demonstrate that the intra-complex mode of dimerization predominates in the eukaryotic Mre11 complex, providing the first structural distinction between the bacterial and eukaryal complexes. We identified a novel eukaryotic-specific interface within the hook proximal coiled-coils that acts coordinately with the Rad50 hook domain to stabilize the intra-complex assembly (Fig. 7a). Both the intra-complex assembly and the Rad50 coiled-coil interface appear to be unique to eukaryotic Rad50. However, recent structural information regarding archaeal as well as eukaryal SMC family members reveal analogous “rod-shaped” assemblies which similarly include coiled-coil interfaces adjacent to their respective apexes[37]. This suggests that the bacterial Rad50 orthologs may be outliers in evolutionary terms, and thus appear more distantly related to the SMC family than their eukaryal counterparts.

A crystal structure of the human Rad50 apex comprising 182 residues reveals that the apex predominantly forms a rod-shaped intra-complex structure stabilized by the hook- and coiled-coil interfaces. Two lines of genetic evidence support the interpretation that the coordinate actions of these domains are required for Mre11 complex functions. First, whereas *rad50ΔCC* and *rad50-48* mutants were individually proficient in SCR, the *rad50ΔCC rad50-48* double mutant exhibited pronounced clastogen sensitivity (Fig. 5a, b). These data suggest that the coiled-coil interface can partially compensate for defects in the hook interface. This compensation likely also underlies the SCR proficiency of *rad50-46* and *-47*[20]. Second, the *rad50*$^{sc+h}$ mutant, which lacks the coiled-coil interface, exhibited largely wild type SCR levels; however, when combined with loss of the hook domain in *rad50*^{sc}, SCR was abolished[25]. Finally, the coiled-coil interface is unlikely to be a transient contact, because the SMC hinge and *Pf*hook substitution mutants which preclude formation of the interface are highly defective in all Mre11 complex functions (Fig. 5, 6). The stability of the coiled-coil interface also undermines the possibility that the complex may switch between the intra- and inter-complex modes of assembly (Supplementary Note 2).

The structure revealed an additional novel feature—a highly flexible hinge loop domain situated below the coiled-coil interface (Fig. 2f, Supplementary Fig. 2a). Notably, Ser635 which falls within the hinge loop is a site of ATM-dependent phosphorylation, which appears to influence DNA repair and cell cycle checkpoint in human cells, supporting the importance of the hinge loop for Rad50 functions[38]. Structural and biochemical analyses of the Mre11 complex globular domains from *M. jannaschii*, *P. furiosus* and *T. maritima* revealed that ATP binding and hydrolysis is associated with large scale conformational transitions, defining closed (ATP bound) and open (ATP hydrolyzed) forms of the complex[5,6,9,16,17]. The data further suggest that the closed form of the complex mediates end binding and likely promotes NHEJ and ATM/Tel1 activation, whereas the open form renders the Mre11 nuclease active site accessible and thus promotes DNA end processing[5,6,16]. In this context, we propose that the flexible hinge loop is required to accommodate ATP dependent conformational transitions. The coiled-coil interface also influences ATP hydrolysis and DNA binding, as Rad50ΔCC and Rad50ΔCC-48 mutants exhibited defects in both activities (Fig. 6d). Those defects were not associated with reduced ATP binding,

indicating that the closed form of the complex is likely to be hyperstabilized in those mutants.

On the other hand, data presented here and elsewhere support the interpretation that the hook and coiled-coil domains influence the disposition of the globular domain in manner that does not rely on ATP hydrolysis. For example, there are only minor differences in ATP binding between Rad50ΔCC and Rad50ΔCC-48 while both exhibit significant reduction in ATPase activity (Fig. 6d). Nevertheless, the two mutants exhibited notable functional differences. Moreover, we have shown that the phenotype of hook domain (*rad50-46*, *-47*, and *-48*)[20] as well as ΔCC-48 mutants (data not shown) can be suppressed by mutations affecting residues in the coiled-coils. One of the suppressor mutations (N607Y) for the *rad50-46* mutant strain is located at the coiled-coil region[20] (Supplementary Fig. 6). This suppressor encodes a residue whose side chain could face each other and move the two coiled-coils closer, further supporting a model that the coiled-coil interface stabilizes the homo-dimerization. Overall, the data indicate that the hook, coiled interface, the hinge loop, and the coiled-coil domains collectively influence functions specified within the globular domain and can exert that influence independently of ATP hydrolysis.

The data presented strongly favor the intra-complex as the predominant form of the complex. We cannot rigorously exclude the possibility that an inter-complex can form. Indeed, it has been observed in EM and AFM analysis, although in no instance was it the predominant form[21,27] and in light of previous data[20], its functional significance remains unclear. How, then, might the Mre11 complex facilitate SCR? The Mre11 complexes are known to oligomerize via apex, coiled-coils, and globular domains[15,39]. It is possible that the complex increases the local concentration of the globular domain through oligomerization and locates the bound DNA molecules in relatively close distances, which may facilitate SCR or other repair functions (Fig. 7b). In addition, loading of cohesin at DNA damage sites is Mre11 complex-dependent[40,41] and we have previously suggested that this may provide sufficient bridging of sister chromatids to promote SCR. Assuming that the intra-complex could achieve this recruitment, this notion could at least partially account for the SCR proficiency *rad50hook* alleles[20].

It is notable that a role for the Mre11 complex in activating DNA damage signaling is confined to eukaryotes and coincides with three structural features that distinguish the eukaryal versions of the Mre11 complex. The inclusion of Nbs1/Xrs2 as a third member of the complex is unique to eukarya[8,36,42,43]. The presence of the coiled-coil interface in Rad50 is also confined to eukarya. Mutation of the coiled-coil interface had a circumscribed effect, leaving DNA repair functions intact, but strongly impairing Tel1 activation. This observation demonstrates the importance of the coiled-coil interface for ATM/Tel1 activation, and support the view that these structural features coordinately underlie Mre11 complex-dependent activation of the ATM/Tel1 kinase (Fig. 7a).

ONLINE METHODS

Protein construction, expression and purification

For crystallization and biochemical analyses, a gene encoding human Rad50 HCC182 (residues 585 to 766) was amplified by PCR and inserted into pET28a. *Escherichia coli* BL21 (DE3) containing the plasmid was grown in LB broth. Zn^{2+} was added to the medium during expression of *Hs*Rad50HCC182 and this construct forms a stable dimer judged from ultracentrifugation analyses (Supplementary Fig.1a). His-tagged protein was purified by Ni^{2+}-NTA affinity chromatography. Fractions containing Rad50HCC182 were further purified by anion exchange chromatography and gel filtration chromatography using a buffer containing 20 mM Tris-HCl pH 7.4, 150 mM NaCl, 5 mM DTT, and 5% glycerol. The SMC hinge, ΔCC, -48 and ΔCC-48 mutants were purified using a virtually identical protocol as WT Rad50HCC182. For SAXS analysis, a gene encoding *Pf*Rad50HCC (residues 351 to 532) was amplified by PCR and inserted into pET28a. The proteins were purified using the same procedure as that of Rad50HCC182.

For FRET experiment, WT and mutant Rad50 constructs were obtained either in bacterial system or via chemical synthesis using microwave-assisted peptide synthesizer (CEM Liberty system). WT (651–722) protein with N-terminal cysteine was produced using IMPACT (Intein Mediated Purification with an Affinity Chitin-binding Tag) system. *Pf*hook protein with N-terminal cysteine was obtained by the modification of pET-28a with the putative thrombin cleavage site LVPRG to LVPRC. All constructs contained N-terminal cysteine required for further native chemical ligation (NCL hereinafter)[44]. Briefly, a gene encoding human Rad50 (651–722) was amplified by PCR and inserted into pTWIN1 for N-terminal cysteine to use in NCL reaction. *E. coli* BL21 (DE3) containing the plasmid was grown in LB broth. Chitin binding domain (CBD)-tagged protein was loaded onto the chitin column with a buffer containing 20 mM Tris-HCl pH 8.5, 500 mM NaCl and 0.05 mM TCEP. On column cleavage of the Intein-tag fused Rad50 (651–722) was performed with a buffer containing 20 mM Tris-HCl pH 7.0, 500 mM NaCl and 0.05 mM TCEP at room temperature for 40 hours. WT and *Pf*hook proteins with N-terminal cysteine were further purified by reversed-phase HPLC on Phenomenex Aeris Peptide XB-C18 column using 0.1 % trifluoroacetic acid (TFA) with an acetonitrile gradient. The purified protein was identified by ESI mass spectrometry with an API2000 Applied Biosystems instrument.

Synthesis of ΔCC construct was performed in two steps by the initial synthesis of two shorter peptides (peptide 1 (585–680Δ614–668) and peptide 2 (681–766Δ702–750)) and following NCL reaction to obtain final product. Peptide 1 and peptide 2 of ΔCC and ΔCC-48 proteins were synthesized on solid phase using Fmoc strategy in microwave-assisted automated peptide synthesizer (CEM Liberty 1) and purified by RP-HPLC[44]. All of proteins prepared for FRET analysis were N-terminally labeled with dansyl chloride (DNS), 5(6)-carboxyfluorescein (FAM) or 5(6)-carboxytetramethylrhodamine (TAMRA) by the NCL28[28,44]. NCL approach involves ligation of a peptide possessing N-teminal Cys and C-terminally activated peptide with N-acylurea moiety (Nbz), represented in this study by DNS/FAM/TAMRA-Ser-Gly_{Nbz}.

For ATP binding and hydrolysis assays, human Mre11 complex was purified from Sf9 cells as described by Lee and Paull[45]. Expression constructs for wild-type MRN were gifts from T. Paull. Wild-type and mutant MRN complexes were expressed in Sf9 insect cells by co-expression with baculovirus prepared from the transfer vectors pTP813 (wild-type Mre11), pTP284 (wild-type Nbs1), and pTP11 (wild-type Rad50) or various Rad50 mutants as described previously[15,46].

Crystallization and data collection

Crystals of the human Rad50HCC182 were grown at 20°C by a hanging drop vapor diffusion method. The crystallization buffer contained 28 – 30% polyethylene glycol 600, 0.1 M bis-tris propane pH 8.7, 3% 1, 6-hexanediol, and 5 mM DTT. Diffraction data were collected at −170°C using crystals flash-frozen in crystallization buffer containing 20% glycerol. Diffraction data were collected 0.9766 Å on a Beamline 5C apparatus at the Pohang Advanced Light Source. The Rad50HCC182 crystals formed in the space group $P2_1$ with a = 42.2 Å, b = 62 Å, c = 81.5 Å, and β = 99.8°. Crystals contained two Rad50 molecules in an asymmetric unit. Diffraction data integration, scaling, and merging were performed using the HKL2000 package[47] (Table 1).

Structure Determination and refinement

Structure of the *Hs*Rad50HC182C was determined by the single-wavelength anomalous scattering dispersion method using the program PHENIX[48]. After density modification including solvent flattening, and electron density map generated at a resolution of 3.0 Å using PHENIX provided a good electron density map[48]. Successive rounds of model building using COOT[49] and refinement using PHENIX[48] were used to build the complete model. A restrained non-crystallographic symmetry was applied throughout the refinement process. Prior to refinement, 5% of the reflections were randomly omitted to monitor the R_{free} value. Details of refinement statistics are summarized in Table 1.

Mutagenesis

We designed coiled-coil deletion (ΔCC) and hook substituted version of Rad50HCC. Residues (614–668, 702–750) were deleted for the ΔCC mutant. For the Rad50-48 mutant, Ser679 and Pro682 were mutated to arginine. For the ΔCC-48 mutant, the Rad50-48 mutation was combined to ΔCC. See Supplementary Table 4 for further information.

Crosslinking analysis

K599C or S738C were introduced to wild-type, SMC hinge- and *Pf*hook-substituted mutants. K599C was introduced to ΔCC, Rad50-48 and ΔCC-48 for the crosslinking analysis. All cysteine-introducing mutants were purified under reducing conditions (1 mM DTT) and diluted 5-fold in the buffer containing 25 mM Tris-HCl pH7.4, 150 mM NaCl and 5% glycerol for assay. H_2O_2 were diluted to a concentration of 2 mM prior to cross-linking reaction. After 5 min incubation at 23°C, samples were run on SDS-PAGE followed by Coomassie blue staining. The crosslinking agents were dissolved to a concentration of 40 mM in DMSO just before use and diluted to 2 mM in cross-linking reaction buffer. After 5 min incubation at 23°C, 5 mM cysteine was added to stop the reaction and samples were

further incubated for 15 min. Samples of stopped reactions were run on SDS-PAGE followed by Coomassie blue staining.

ATP binding and hydrolysis assay

For ATP binding and hydrolysis assays, various human MRN complexes were incubated in 10 μl reactions containing buffer A (25 mM MOPS-NaOH, pH 7.0, 50 mM NaCl, 1 mM DTT) with 5 mM $MgCl_2$ and 12.5–100 uM ATP containing 150 nM [γ-^{32}P]ATP. Reactions were incubated at 30°C for 2.5, 7.5, 15, 30 or 60 min and were stopped with the addition of 1% SDS and 10 mM EDTA. The reaction (2 μl) was then spotted on a polyethyleneimine (PEI) plate (EMD Biosciences) and separated by TLC for ATP, ADP, and P_i by using 0.75 M KH_2PO_4 (pH 3.4). The plates were dried and analyzed by Typhoon imager (GE). The levels of P_i generated were used as a measure of ATPase activity.

SAXS

Small-angle X-ray scattering (SAXS) measurements were performed at the 4C SAXS II beamline of the Pohang Light Source II. A light source from an In-vacuum Undulator 20 (IVU20) was focused with a vertical focusing toroidal mirror coated with rhodium and monochromatized with a Si (111) double crystal monochromator (DCM), yielding an X-ray beam wavelength of 0.734 Å. The X-ray beam size at the sample stage was 0.1 (V) × 0.3 (H) mm^2. A two-dimensional (2D) charge-coupled detector (Mar USA, Inc.) was employed. A sample-to-detector distance of 4.00 m and 1.00 m for SAXS were used. The magnitude of scattering vector, $q = (4\pi/\lambda) \sin 2\theta$, was 0.1 nm^{-1} < q < 6.50 nm^{-1}, where 2θ is the scattering angle and λ is the wavelength of the X-ray beam source. The scattering angle was calibrated with polystyrene-b-polyethylene-b-polybutadiene-b-polystyrene block copolymer standard. We used quartz capillary with an outside diameter of 1.5 mm and wall thickness of 0.01 mm, as solution sample cells. All scattering measurements were carried out at 4°C by using a FP50-HL refrigerated circulator (JULABO, Germany). The SAXS data were collected in six successive frames of 0.1 min each to monitor radiation damage. Measurements of protein solutions were carried out over a small concentration range 1~5 mg/ml. Each 2D SAXS pattern was radial averaged from the beam center and normalized to the transmitted X-ray beam intensity, which was monitored with a scintillation counter placed behind the sample. The scattering of specific buffer solutions was used as the experimental background.

Analytical ultracentrifuge

Molecular mass of the Rad50HCC182 was analyzed with an Optima XL-A analytical ultracentrifuge (Beckman). Sedimentation equilibrium data were evaluated using a nonlinear least-squares curve-fitting algorithm (XL-A data analysis software). Samples (40 μM) were analyzed in a buffer B (25 mM Tris-HCl pH 7.4, 150 mM NaCl, 5 mM β-mercaptoethanol) for Rad50HCC182, SMC hinge, *Pf*hook, ΔCC, and ΔCC-48 or buffer C (buffer B with 0.5 mM EDTA) for Zn^{2+}-free Rad50HCC182. To prepare Zn^{2+} free Rad50HCC182, sample was dialyzed in a buffer C for at least 24 hrs. Data were collected at 11,000, 14,000, 25,000, 35,000, and 37,000 rpm to optimize the detection of dimeric and monomeric Rad50HCC182 mutants and 15°C using an An60Ti rotor (Beckman) and by measuring the absorbance at 280 nm. The partial specific volume of Rad50HCC182 was estimated to be 0.731 cm^3/g

from the protein sequence using the SEDNTERP program, and a rho value of 1.005 was used for the molecular mass calculation. The partial specific volume of SMC hinge, *Pf*hook, ΔCC, and ΔCC-48 were estimated to be 0.738, 0.734, 0.722, and 0.721 cm^3/g, respectively.

DNA binding assay

Gel mobility shift assay was performed with a 83 mer dsDNA substrate composed of 5' [^{32}P]-labeled Top strand (5′-TTG ATA AGA GGT CAT TTT TGC GGA TGG CTT AGA GCT TAA TTG CTG AAT CTG GTG CTG TAG CTC AAC ATG TTT TAA ATA TGC AA-3′) annealed to its complementary bottom strand. 0 – 800 nM MRN complexes were incubated with 3 nM DNA substrate in 10 ul reactions in the presence of 25 mM Tris-Cl (pH 7.6), 7.5% glycerol, 50 mM NaCl, 1 mM β-mercaptoehtanol, 0.1% Igepal, 0.1 mg/ml BSA, 5 mM $MgCl_2$ and 0.5 mM AMP-PNP for 20min at RT. The reactions were resolved by 5% native polyacrylamide gel electrophoresis in 1× TAE buffer supplemented with 1.5 mM $MgCl_2$and gels were dried and analyzed by Typhoon imager (GE).

Mutant protein structural changes

Structural changes in the mutants (5 μM) versus the wild type Rad50HCC were monitored by CD spectrophotometer (Jasco J-715) at wavelength range of 200–260 nm. All samples were prepared in the buffer 20 mM Tris-HCl (pH 7.4), 150 mM NaCl, 5 mM β-mercaptoethanol and 5% glycerol.

Protein equilibration in metal buffers

The Zn^{2+}-dependent dimerization of fluorescently labeled zinc hook peptides (Supplementary Table 4) was monitored by fluorescence resonance energy transfer measurements in a series of metal buffers (Supplementary Table 3). Extremely high affinity of zinc hook motif towards Zn^{2+} dictates the necessity of applying strict control of the free zinc concentration[28]. To determine the dissociation constants and associated conformational changes of peptide/protein, we applied three common zinc chelators (EDTA, HEDTA, and EDDS) for which stability of ZnL complexes are well established[50]. Apparent pK_d of Zn^{2+} complex with EDTA, HEDTA and EDDS at pH 7.4 (I = 0.1 M) is 13.6, 12.2 and 10.6, respectively. By mixing 1 mM of each chelator with Zn^{2+} to final concentrations of $ZnSO_4$ from 0.05 to 0.9 mM we were able to create strictly buffered free zinc conditions that can be described via pZn parameter, analogous to pH[51]. Supplementary Table 2 shows pZn values for all zinc buffers used in our studies (50 mM Hepes-NaOH, pH 7.4, 150 mM NaCl, 0.2 mM TCEP, I = 0.1 M). The range and choice of the chelators is selected based on previous studies with zinc hook domain[20,28]. Accurate free Zn^{2+} values were calculated based on protonation constants of EDTA, HEDTA, EDDS, and their stability constants with Zn^{2+} using the program HySS2009[51,52] (Supplementary Table 2).

FRET analysis

To study the formation of Zn^{2+} complexes of Rad50 constructs we have prepared initially equimolar mixture of two proteins that forms FRET pair with each other (donor and acceptor). In all cases 20 μM mixture of two differently modified proteins (DNS/FAM and FAM/TAMRA) have been incubated with metal buffers in the total reaction volume of 1.4

ml for the period of 4h and measured. Additional measurements were taken after 12h. Steady-state fluorescence measurements were obtained using a FluoroMax-4 spectrofluorimeter (Jobin Yvon Horiba) equipped with Peltier-thermostatted cell holder. FRET measurements of DNS and FAM labeled proteins incubated in a series of metal buffers controlling free Zn^{2+} were performed with the excitation and emission wavelengths set to λ_{ex} = 350 nm and λ_{em} = 520 nm. The pZn values obtained from data fitting to Hill's equation allows to calculated dissociation constant according to procedure described in our previous report[20,28]. Briefly, the inflection points correspond to the formation of ½ of total homodimer, equal to 5 nM concentration. Free protein is 10 nM and free Zn^{2+} is 10^{-pZn} from the experiment. FRET measurements of the other FRET pair, FAM-Rad50 and TAMRA-Rad50, were conducted using higher labeled protein concentration, namely 250 nM, due to significant FRET efficiency dependence on acceptor concentration. The excitation and emission wavelengths were set to λ_{ex} = 492 nm and λ_{em} = 580 nm for aforementioned mixture.

Distance calculation between Donor and Acceptor

FRET efficiency was calculated using equation below based on following considerations.

$$E=1-(F_{DA}/F_D)=1-((F_{obs}-0.5\times F_D)/F_D)$$

where F_{DA}: emission intensity of the donor with the acceptor present; F_D: emission intensity of the donor alone; F_{obs}: observable emission intensity of the donor with the acceptor present. We have focused on the spectral changes in the 480 nm range – a range specific for the DNS group emission excluding the FAM emission from the calculations. Also, due to the heterogeneity of the fluorescently labeled dimers, we took into account that only 50% of the fluorophore is involved in the observed FRET. We estimated the actual distance between two fluorophores in the dimer using above equation and the formula describing the correlation between the efficiency and the Förster distance (R_0).

$$R=[(R_0{}^6/E)-R_0{}^6]^{1/6} \text{or } E=R_0{}^6/[R_0{}^6+R^6];$$

$$\text{distance } (0.5\times R_0{}^6<R<1.5\times R_0{}^6)$$

The Förster distance (R_0 value) was calculated from following equation:

$$R_0=0.211\times[k^2\Phi_D n^{-4}J(\lambda)]^{1/6}[\text{in } \mathring{A}]$$

Where k^2 is the orientation factor for the emission and absorption dipoles and its value depends on their relative orientation. We used k^2 = 2/3 which is the value for random orientation of donor and acceptor molecules. Φ_D is the quantum yield of donor (0.11 for DNS and 0.75 for FAM). n is refractive index of the water medium which is 1.57. $J(\lambda)$ is the overlap integral of the fluorescence emission spectrum of donor and the absorption spectrum

of the acceptor. The $J(\lambda)$ and R_0 values determined are shown in Supplementary Table 3. The values are in the typical range of DNS-FAM and FAM-TAMRA FRET pair ranges. Supplementary Table 3 also shows calculated distances between donor and acceptor groups attached to the N-termini of the Rad50 protomers of the dimer calculated based on the equation described above and emission intensities measured during the FRET experiments.

Other yeast manipulations

Most experiments (unless specified otherwise) were performed with yeast strains in which the *rad50* alleles were integrated at the native locus with the *HYG* resistance marker in the 3' UTR (*rad50::HYG*) and grown in YPD media containing Hygromycin B (300 μg/ml). In some experiments, Rad50 was also expressed in haploid or diploid *rad50Δ* cells from the single copy centromeric plasmid *Ycp50* (*URA3*) under control of its native promoter in dropout media without uracil (Do-Ura). Strains were genotyped by PCR sequencing to confirm the presence of the *rad50* alleles. All experiments were performed with minimally two independent yeast strains of each genotype. Yeast strains used in this study are listed in Supplementary Table 5. In DNA damage survival assays, cells were grown at 30°C to stationary phase, serially 5-fold diluted and were spotted (250,000 to 80 cells) onto freshly prepared YPD plates containing the indicated concentrations of MMS or CPT. Yeast strains, in which HO-DSB formation at the *MAT* locus is regulated by the *GAL* promoter, were grown in YEPEG media (1% yeast extract, 2% peptone, 2.6% glycerol, 2.6% ethanol and 1% succinic acid, all wt/vol). HO-DSB formation was induced upon addition of galactose and sucrose (both 2% final concentration) to exponentially (2×10^7 cells/ml) growing cells for 2 hr in liquid culture, or in presence of 2% glucose and 2% sucrose in absence of HO expression. Cell survival was determined as previously described[25]. Co-immunoprecipitation was performed essentially as described[25] using Recombinant Protein G-Sepharose 4B (ThermoFisher) pre-blocked with 5% (wt/vo) BSA, incubated for 6 hr with anti-Rad50 (64911) or anti-Mre11 (59567) antisera and overnight with 3 mg clarified yeast extracts, and western blotting (nitrocellulose membrane) with anti-Rad50, anti-Mre11, anti-Xrs2 (UWM45) and protein A/G-HRP conjugated (Pierce).

To assess sporulation efficiencies and spore viability, *rad50Δ/Δ* (W303+) containing various *Ycp50-rad50* plasmids, were grown in Do-Ura media and then diluted for 14 hr in Do-Ura media with 2% (wt/vol) potassium acetate (pre-sporulation media). The cells were collected and washed with water and re-suspended in sporulation media (1% Potassium acetate, 0.02% Raffinose) and cultivated for another 48 hr. From these sporulated cultures, sporulation efficiencies were determined by counting the number of tetrads observed among at least 264 cells in bright field microscopy, and spore viability by tetrad dissection of at least 27 tetrads.

FLAG-Rad53-phosphorylation was assessed as previously described[53] with minor modifications. Exponentially growing cells were incubated for 90 min with 0.15% MMS, treated with 10% thiosulfate, and protein extract were made by TCA-extraction. 20 μg extract were separated on an 7.5% SDS-PAGE (14 cm × 16 cm, 6 hr at 120 V) and transferred to a nitrocellulose membrane probed with FLAG M2 mAb (Sigma) and anti-mouse horseradish peroxidase conjugate (HRP; Pierce) and visualized by chemifluorescence

using the ECL Prime Kit (Amersham). Telomere southern blot were done as previously described using PstI-digested genomic DNA and a telomere-specific probe[25].

Supplementary Material

Refer to Web version on PubMed Central for supplementary material.

Acknowledgments

We thank Tomasz Kochańczyk for discussions and information regarding fluorescent protein modification and members of the Cho and Petrini labs for helpful comments throughout. This work was supported by grants from the National Research Foundation of Korea (NRF) funded by the Korea Government (MEST, No. 2015R1A2A1A05001694), and BK21 Program (Ministry of Education) to Y.C.; NIH RO1 grant GM56888 (J.H.J.P.) and the MSK Cancer Center Core Grant P30 CA008748; National Science Center, Poland (Opus, No. 2014/13/B/NZ1/ 00935) to A.K.

References

1. Schiller CB, et al. Structure of Mre11-Nbs1 complex yields insights into ataxia-telangiectasia-like disease mutations and DNA damage signaling. Nat. Struct. Mol. Biol. 2012; 19:693–700. [PubMed: 22705791]
2. de Jager M, et al. Differential arrangements of conserved building blocks among homologs of the Rad50/Mre11 DNA repair protein complex. J. Mol. Biol. 2004; 339:937–949. [PubMed: 15165861]
3. Hirano T. At the heart of the chromosome: SMC proteins in action. Nat. Rev. Mol. Cell. Biol. 2006; 7:311–322. [PubMed: 16633335]
4. Wyman C, Lebbink J, Kanaar R. Mre11-Rad50 complex crystals suggest molecular calisthenics. DNA Repair (Amst.). 2011; 10:1066–1070. [PubMed: 21893433]
5. Deshpande RA, et al. ATP-driven Rad50 conformations regulate DNA tethering, end resection, and ATM checkpoint signaling. EMBO J. 2014; 33:482–500. [PubMed: 24493214]
6. Liu Y, et al. ATP-dependent DNA binding, unwinding, and resection by the Mre11/Rad50 complex. EMBO J. 2016; 35:743–758. [PubMed: 26717941]
7. Paull TT, Gellert M. Nbs1 potentiates ATP-driven DNA unwinding and endonuclease cleavage by the Mre11/Rad50 complex. Genes. Dev. 1999; 13:1276–1288. [PubMed: 10346816]
8. Stracker TH, Petrini JH. The MRE11 complex, starting from the ends. Nat. Rev. Mol. Cell. Biol. 2011; 12:90–103. [PubMed: 21252998]
9. Lim HS, Kim JS, Park YB, Gwon GH, Cho Y. Crystal structure of the Mre11-Rad50-ATPγS complex: understanding the interplay between Mre11 and Rad50. Genes. Dev. 2011; 25:1091–1104. [PubMed: 21511873]
10. Möckel C, Lammens K, Schele A, Hopfner KP. ATP driven structural changes of the bacterial Mre11:Rad50 catalytic head complex. Nucleic Acids Res. 2012; 40:914–927. [PubMed: 21937514]
11. Rojowska A, et al. Structure of the Rad50 DNA double-strand break repair protein in complex with DNA. EMBO J. 2014; 33:2847–2859. [PubMed: 25349191]
12. Seifert FU, Lammens K, Stoehr G, Kessler B, Hopfner KP. Structural mechanism of ATP-dependent DNA binding and DNA end bridging by eukaryotic Rad50. EMBO J. 2016; 35:759–772. [PubMed: 26896444]
13. Sung S, et al. DNA end recognition by the Mre11 nuclease dimer: insights into resection and repair of damaged DNA. EMBO J. 2014; 33:2422–2435. [PubMed: 25107472]
14. Williams RS, et al. Mre11 dimers coordinate DNA end bridging and nuclease processing in double-strand-break repair. Cell. 2008; 135:97–109. [PubMed: 18854158]
15. Lee JH, et al. Ataxia telangiectasia-mutated (ATM) kinase activity is regulated by ATP-driven conformational changes in the Mre11/Rad50/Nbs1 (MRN) complex. J. Biol. Chem. 2013; 288:12840–12851. [PubMed: 23525106]

16. Lammens K, et al. The Mre11, Rad50 structure shows an ATP-dependent molecular clamp in DNA double-strand break repair. Cell. 2011; 145:54–66. [PubMed: 21458667]
17. Williams GJ, et al. ABC ATPase signature helices in Rad50 link nucleotide state to Mre11 interface for DNA repair. Nat. Struct. Mol. Biol. 2011; 18:423–431. [PubMed: 21441914]
18. Lafrance-Vanasse J, Williams GJ, Tainer JA. Envisioning the dynamics and flexibility of Mre11-Rad50-Nbs1 complex to decipher its roles in DNA replication and repair. Prog. Biophys. Mol. Biol. 2015; 117:182–193. [PubMed: 25576492]
19. Barfoot T, et al. Functional Analysis of the Bacteriophage T4 Rad50 Homolog (gp46) Coiled-coil Domain. J. Biol. Chem. 2015; 290:23905–23915. [PubMed: 26242734]
20. Hohl M, et al. Interdependence of the rad50 hook and globular domain functions. Mol. Cell. 2015; 57:479–491. [PubMed: 25601756]
21. Hopfner KP, et al. The Rad50 zinc-hook is a structure joining Mre11 complexes in DNA recombination and repair. Nature. 2002; 418:562–566. [PubMed: 12152085]
22. Wiltzius JJ, Hohl M, Fleming JC, Petrini JH. The Rad50 hook domain is a critical determinant of Mre11 complex functions. Nat. Struct. Mol. Biol. 2005; 12:403–407. [PubMed: 15852023]
23. Roset R, et al. The Rad50 hook domain regulates DNA damage signaling and tumorigenesis. Genes. Dev. 2014; 28:451–462. [PubMed: 24532689]
24. Bressan DA, Baxter BK, Petrini JH. The Mre11-Rad50-Xrs2 protein complex facilitates homologous recombination-based double-strand break repair in Saccharomyces cerevisiae. Mol. Cell. Biol. 1999; 19:7681–7687. [PubMed: 10523656]
25. Hohl M, et al. The Rad50 coiled-coil domain is indispensable for Mre11 complex functions. Nat. Struct. Mol. Biol. 2011; 18:1124–1131. [PubMed: 21892167]
26. van der Linden E, Sanchez H, Kinoshita E, Kanaar R, Wyman C. RAD50 and NBS1 form a stable complex functional in DNA binding and tethering. Nucleic Acids Res. 2009; 37:1580–1588. [PubMed: 19151086]
27. Moreno-Herrero F, et al. Mesoscale conformational changes in the DNA-repair complex Rad50/Mre11/Nbs1 upon binding DNA. Nature. 2005; 437:440–443. [PubMed: 16163361]
28. Kochańczyk T, Jakimowicz P, Krężel A. Femtomolar Zn(II) affinity of minimal zinc hook peptides--a promising small tag for protein engineering. Chem. Comm. (Camb). 2013; 49:1312–1314.
29. Haering CH, Löwe J, Hochwagen A, Nasmyth K. Molecular architecture of SMC proteins and the yeast cohesin complex. Mol. Cell. 2002; 9:773–788. [PubMed: 11983169]
30. Boulton SJ, Jackson SP. Components of the Ku-dependent non-homologous end-joining pathway are involved in telomeric length maintenance and telomeric silencing. EMBO J. 1998; 17:1819–1828. [PubMed: 9501103]
31. Chen L, Trujillo K, Ramos W, Sung P, Tomkinson AE. Promotion of Dnl4-catalyzed DNA end-joining by the Rad50/Mre11/Xrs2 and Hdf1/Hdf2 complexes. Mol. Cell. 2001; 8:1105–1115. [PubMed: 11741545]
32. Moore JK, Haber JE. Cell cycle and genetic requirements of two pathways of nonhomologous end-joining repair of double-strand breaks in Saccharomyces cerevisiae. Mol. Cell. Biol. 1996; 16:2164–2173. [PubMed: 8628283]
33. Keeney S. Spo11 and the formation of DNA double-strand breaks in meiosis. Genome Dyn. Stab. 2008; 2:81–123. [PubMed: 21927624]
34. Usui T, Ogawa H, Petrini JH. A DNA damage response pathway controlled by Tel1 and the Mre11 complex. Mol. Cell. 2001; 7:1255–1266. [PubMed: 11430828]
35. Lee JH, Paull TT. ATM activation by DNA double-strand breaks through the Mre11-Rad50-Nbs1 complex. Science. 2005; 308:551–554. [PubMed: 15790808]
36. Lee JH, et al. Regulation of Mre11/Rad50 by Nbs1: effects on nucleotide-dependent DNA binding and association with ataxia-telangiectasia-like disorder mutant complexes. J Biol Chem. 2003; 278:45171–81. [PubMed: 12966088]
37. Soh YM, et al. Molecular basis for SMC rod formation and its dissolution upon DNA binding. Mol. Cell. 2015; 57:290–303. [PubMed: 25557547]

38. Gatei M, et al. ATM protein-dependent phosphorylation of Rad50 protein regulates DNA repair and cell cycle control. J. Biol. Chem. 2011; 286:31542–31556. [PubMed: 21757780]
39. de Jager M, et al. Human Rad50/Mre11 is a flexible complex that can tether DNA ends. Mol. Cell. 2001; 8:1129–1135. [PubMed: 11741547]
40. Tittel-Elmer M, et al. Cohesin association to replication sites depends on rad50 and promotes fork restart. Mol. Cell. 2012; 48:98–108. [PubMed: 22885006]
41. Unal E, et al. DNA damage response pathway uses histone modification to assemble a double-strand break-specific cohesin domain. Mol. Cell. 2004; 16:991–1002. [PubMed: 15610741]
42. Oh J, Al-Zain A, Cannavo E, Cejka P, Symington LS. Xrs2 Dependent and Independent Functions of the Mre11-Rad50 Complex. Mol. Cell. 2016; 64:405–415. [PubMed: 27746018]
43. Deshpande RA, Lee JH, Arora S, Paull TT. Nbs1 Converts the Human Mre11/Rad50 Nuclease Complex into an Endo/Exonuclease Machine Specific for Protein-DNA Adducts. Mol. Cell. 2016; 64:593–606. [PubMed: 27814491]
44. Blanco-Canosa JB, Dawson PE. An efficient Fmoc-SPPS approach for the generation of thioester peptide precursors for use in native chemical ligation. Angew. Chem. Int. Ed. Engl. 2008; 47:6851–6855. [PubMed: 18651678]
45. Lee J, Paull TT. Purification and biochemical characterization of ataxia-telangiectasia mutated and Mre11/Rad50/Nbs1. Methods Enzymol. 2006; 408:529–539. [PubMed: 16793391]
46. Bhaskara V, et al. Rad50 adenylate kinase activity regulates DNA tethering by Mre11/Rad50 complexes. Mol. Cell. 2007; 25:647–661. [PubMed: 17349953]
47. Otwinowski Z, Minor W. Processing of X-ray diffraction data collected in oscillation mode. Methods Enzymol. 1997; 276:307–326.
48. Adams PD, et al. PHENIX: a comprehensive Python-based system for macromolecular structure solution. Acta. Crystallogr. D Biol. Crystallogr. 2010; 66:213–221. [PubMed: 20124702]
49. Emsley P, Cowtan K. Coot: model-building tools for molecular graphics. Acta. Crystallogr. D Biol. Crystallogr. 2004; 60:2126–2132. [PubMed: 15572765]
50. Martell, AE., Smith, RM. Critical Stability Constants. Plenum Press; New York: 1974.
51. Krężel, A., Maret, W. The biological inorganic chemistry of zinc ions. Arch. Biochem. Biophys. 2016. http://dx.doi.org/10.1016/j.abb.2016.04.010
52. Alderighi L, et al. Hyperquad simulation and speciation (HySS): a utility program for the investigation of equilibria involving soluble and partially soluble species. Coordination Chemistry Reviews. 1999; 184:311–318.
53. Al-Ahmadie H, et al. Synthetic lethality in ATM-deficient RAD50-mutant tumors underlie outlier response to cancer therapy. Cancer Discov. 2014; 4:1014–1021. [PubMed: 24934408]
54. Kozin MB, Svergun DI. Automated matching of high-and low-resolution structural models. J. Appl. Cryst. 2001; 34:33–41.
55. Svergun DI, Barberato C, Koch MHJ. CRYSOL - a Program to Evaluate X-ray Solution Scattering of Biological Macromolecules from Atomic Coordinates. J. Appl. Cryst. 1995; 28:768–773.
56. Svergun DI. Determination of the regularization parameter in indirect-transform methods using perceptual criteria. J. Appl. Crystallogr. 1992; 25:495–503.
57. Sali A, Blundell TL. Comparative protein modelling by satisfaction of spatial restraints. J. Mol. Biol. 1993; 234:779–815. [PubMed: 8254673]

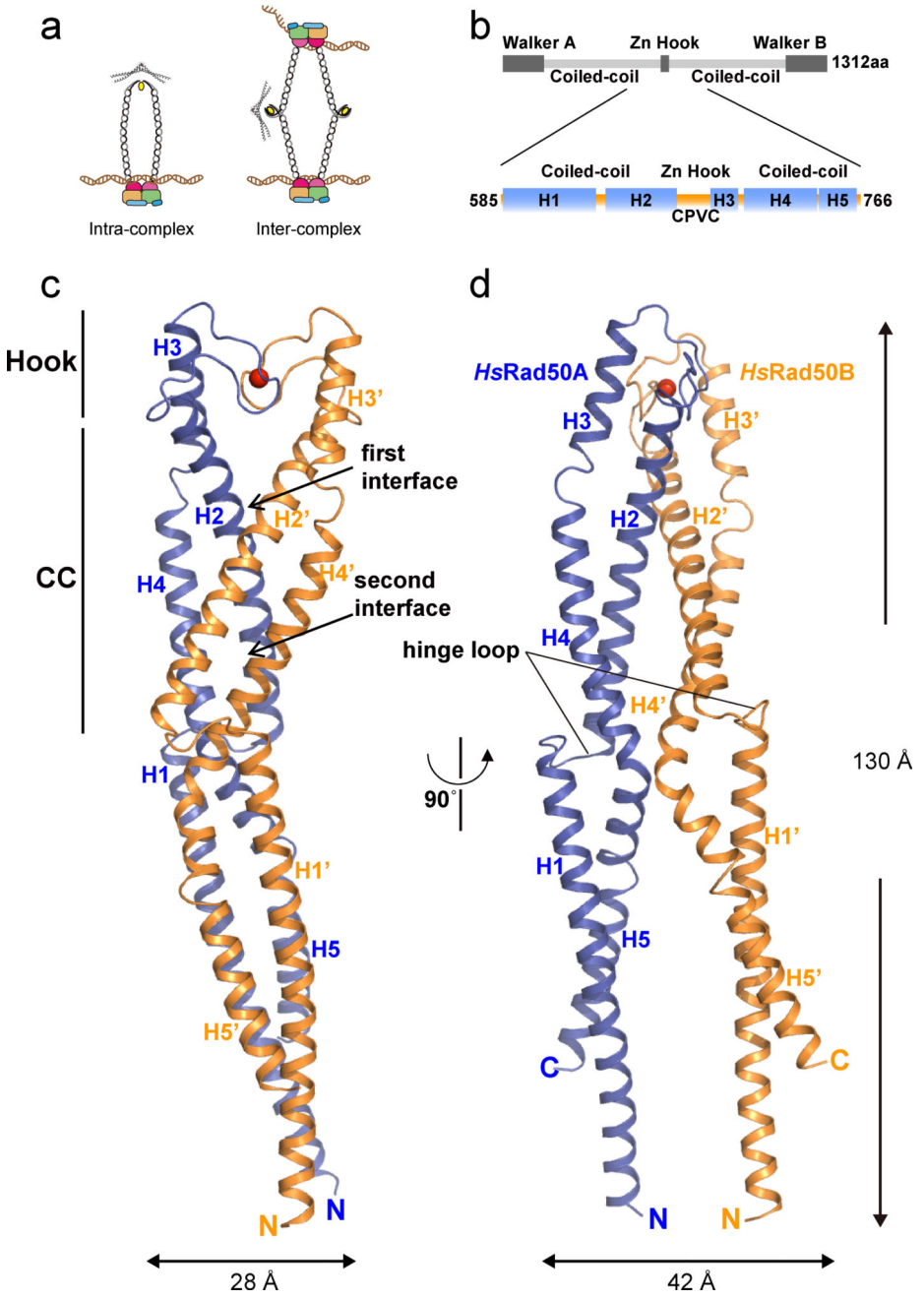

Figure 1. Rod-shaped structure of the Zn^{2+} bound human Rad50 apex dimer

(a) Schematic illustration of the intra-complex (left) and the inter-complex (right) assembly. The rod-shaped and ring-shaped intra-complexes are shown for the intra-complex. Crystal structure of the *Pf*Rad50 hook domain (PDB ID, 1L8D) is shown on top of the ring-shaped intra-complex and at the side of the inter-complex. (b) Domain arrangement of human Rad50 (top) and Rad50HCC182 (bottom). Highly conserved CPVC residues at the hook domain are marked at the bottom. (c, d) Overall structure of the Zn^{2+} (red sphere) -bound Rad50HCC182 dimer in two different views. There are two Rad50HCC182 molecules (Rad50A and Rad50B) in the asymmetric unit. Each monomer is shown in blue (Rad50A)

and orange (Rad50B). The overall dimensions of the *Hs*Rad50HCC182 dimer are 28 × 42 × 130 Å.

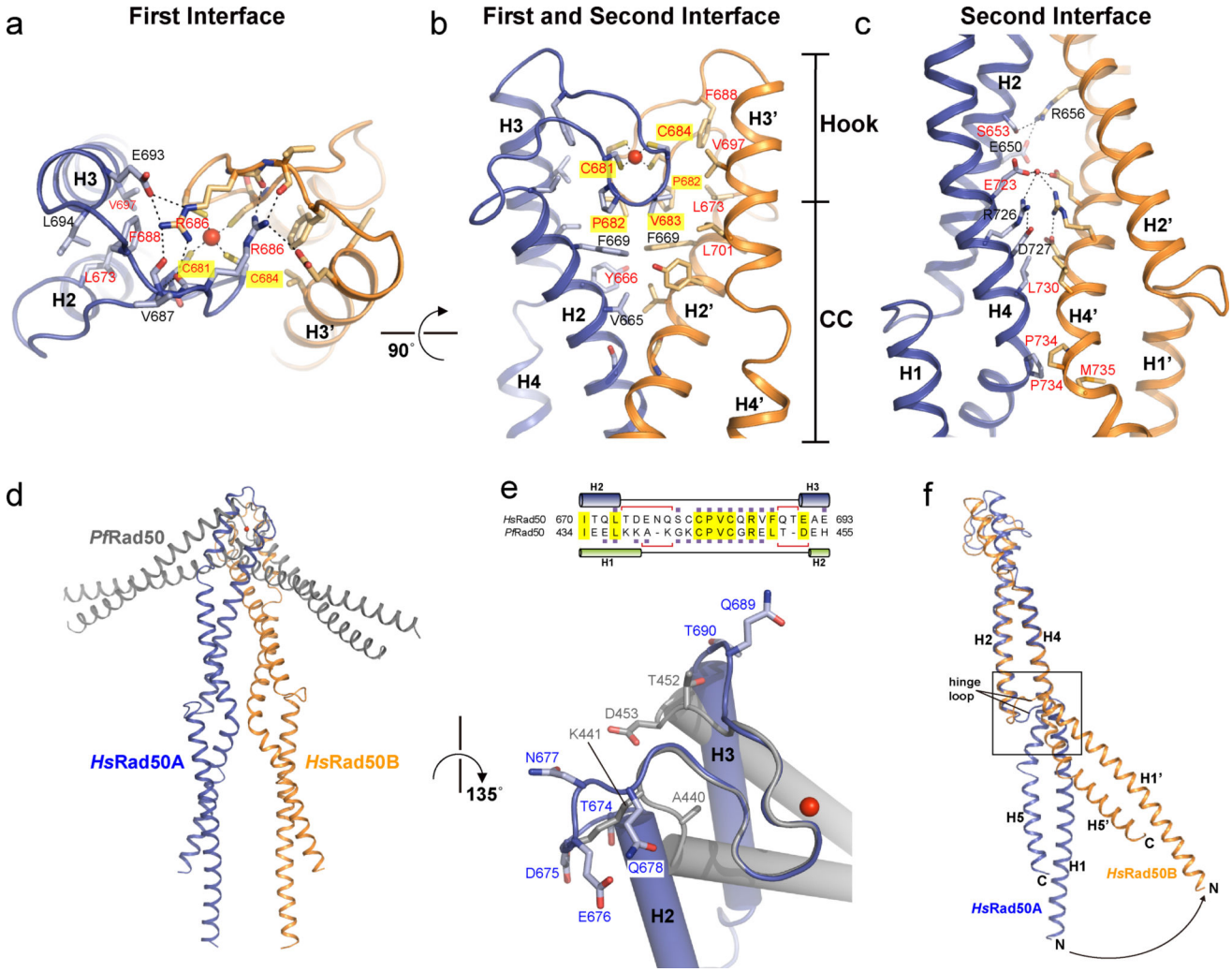

Figure 2. Two interfaces at the apex of *Hs*Rad50 dimer stabilize the rod-shaped structure

(a) Close-up view of the hook interface from the top view of Fig. 1c. Two cysteine residues of each *Hs*Rad50 (Rad50A, blue; Rad50B orange) coordinate one Zn^{2+} ion (red sphere). Highly conserved residues are marked in red. A modeled structure of *S. cerevisiae* Rad50 apex is shown in Supplementary Fig.1d–f. (b) Close-up view of the hook- and coiled-coil interfaces (top half of Fig. 1b) from the side. The Connecting Helices H2 and H3 are tilted to form a hydrophobic cleft (Tyr666, Phe669, Pro682, Val683, Phe688, Val697 and Leu701) where Val683 and Cys684 of another Rad50 molecule fit in. (c) Close-up view of the coiled-coil interface. Dimerization interface is stabilized by ion-pairs between helices H2 and H2' and between H4 and H4' in the middle as well as hydrophobic interactions at each end. (d) Comparison of the overall apex structure between *Hs*Rad50 (blue/ orange) and *Pf*Rad50 (light gray; 1L8D) by aligning ten residues (Cα atoms) at the hook motif. (e) Closed up view of the aligned structures of human Rad50 (blue) and *Pf*Rad50 (light gray). A part of the aligned sequence is shown on top. (f) Comparison of two Rad50HCC182 monomers reveals the flexibility of the hinge loop between helices H1 and H2. Structures of the hook and coiled-coil interfaces are aligned. Helix H1' of *Hs*Rad50B (orange) is rotated about 50° from helix H1 of Rad50A (blue) relative to helix H2.

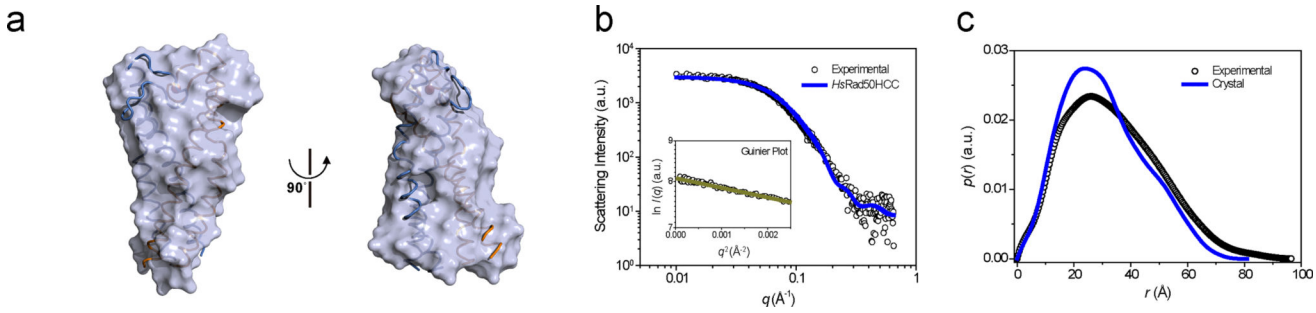

Figure 3. Solution structure of the *Hs*Rad50 apex dimer

(a) Structural superposition of the rod-shaped Rad50HCC complex onto the molecular envelope calculated from the SAXS data showing two different views of the model. To compare the overall shape and dimensions, the crystal models were superimposed onto the solution models using the SUPCOMB program[54]. (b) X-ray scattering profile of *Hs*Rad50HCC protein in solution, which was measured at 4°C. The open symbols are the experimental data and the solid line is theoretical SAXS curve calculated from the crystal structure of *Hs*Rad50HCC dimer using the program CRYSOL[55]. Discrepancy (χ) between the experimental and theoretical curve is 0.32. The Guinier plot of *Hs*Rad50HCC protein is shown in the inset. (c) Pair distance distribution $p(r)$ function for *Hs*Rad50HCC protein, based on an analysis of the experimental SAXS data (empty circles) using the program GNOM[56].

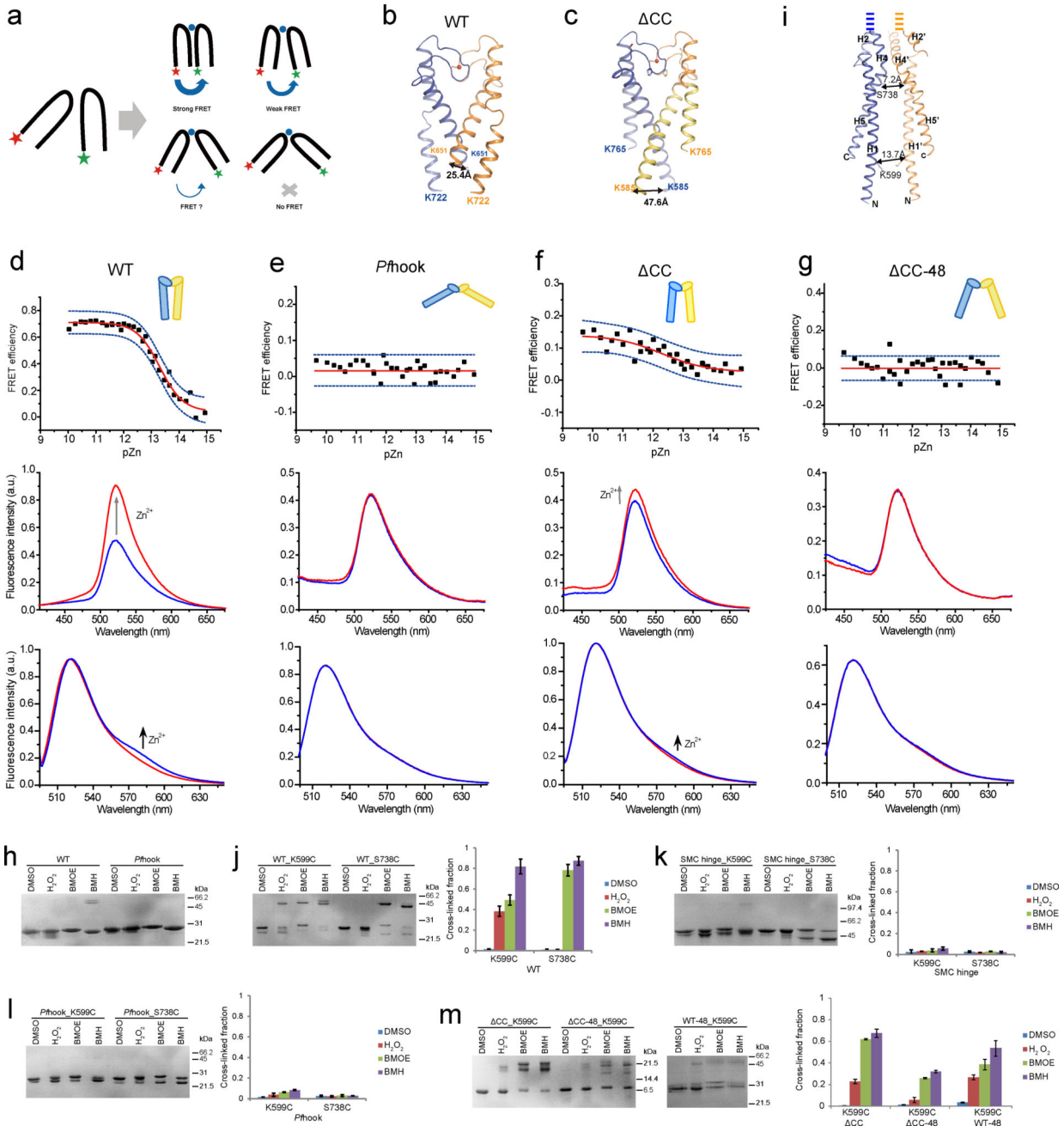

Figure 4. FRET and cosslinking analysis of Rad50HCC WT and mutants

(a) Equilibration of an equimolar mixture of fluorescently modified protein constructs (20 nM DNS-WT and 20 nM FAM-WT or 250 nM FAM-WT and 250 nM TAMRA-WT) with metal buffer. (b) Structure of the wild-type *Hs*Rad50HCC showing the inter-molecular distance between the two N-terminal residues (651). (c) Structure of the *Hs*Rad50HCC ΔCC showing the inter-molecular distance between the two N-terminal residues (585). (d–g) Representative fluorescence spectra of WT and mutant Rad50 apex constructs in zinc buffers together with fluorescence dependence on pZn ($-\log[Zn^{2+}]_{free}$) values. Different zinc buffers provide different zinc buffering and various proteins are saturated at different pZn values. (d)

Top, DNS-FAM WT Rad50HCC emission spectra. FRET efficiency dependence on pZn values and appropriate fit to Hill's equation. Fitted pZn value for the inflection point is 13.30 ± 0.06. Blue dashed line corresponds to 95% data confidence. Middle, DNS-FAM WT Rad50HCC emission spectra. Blue (apo-form) and red (holo-form) spectra were recorded at different pZn values as is provided in the Supplementary Table 2. Bottom, FAM-TAMRA WT Rad50HCC emission spectra. (e) Fluorescence spectra of Rad50 *Pf*hook mutant. (f) Fluorescence spectra of Rad50-ΔCC. Fitted pZn value for the inflection point is 12.3 ± 0.3. (g) Fluorescence spectra of Rad50-ΔCC-48. (h) Crosslink analysis of the intact Rad50HCC182 (left) and *Pf*hook mutant (right) using H_2O_2, BMOE, and BMH. 1% DMSO solution was used for control as BMOE and BMH were dissolved in 1% DMSO. (i) Overall structure of Rad50HCC182 showing the mutated K599C and S738C residues. Distances between the mutated residues are marked. (j–m) Crosslink analysis of K599C (left) and S738C (right) mutant; (j) Rad50HCC182 dimer, (k) the SMC hinge mutant, (l) *Pf*hook mutant, (m) ΔCC (left), ΔCC-48 (middle) and -48 (right). Graph shows the mean +/− s.d. from three independent experiments. Supplementary data set 1 and source data for graphs are available online.

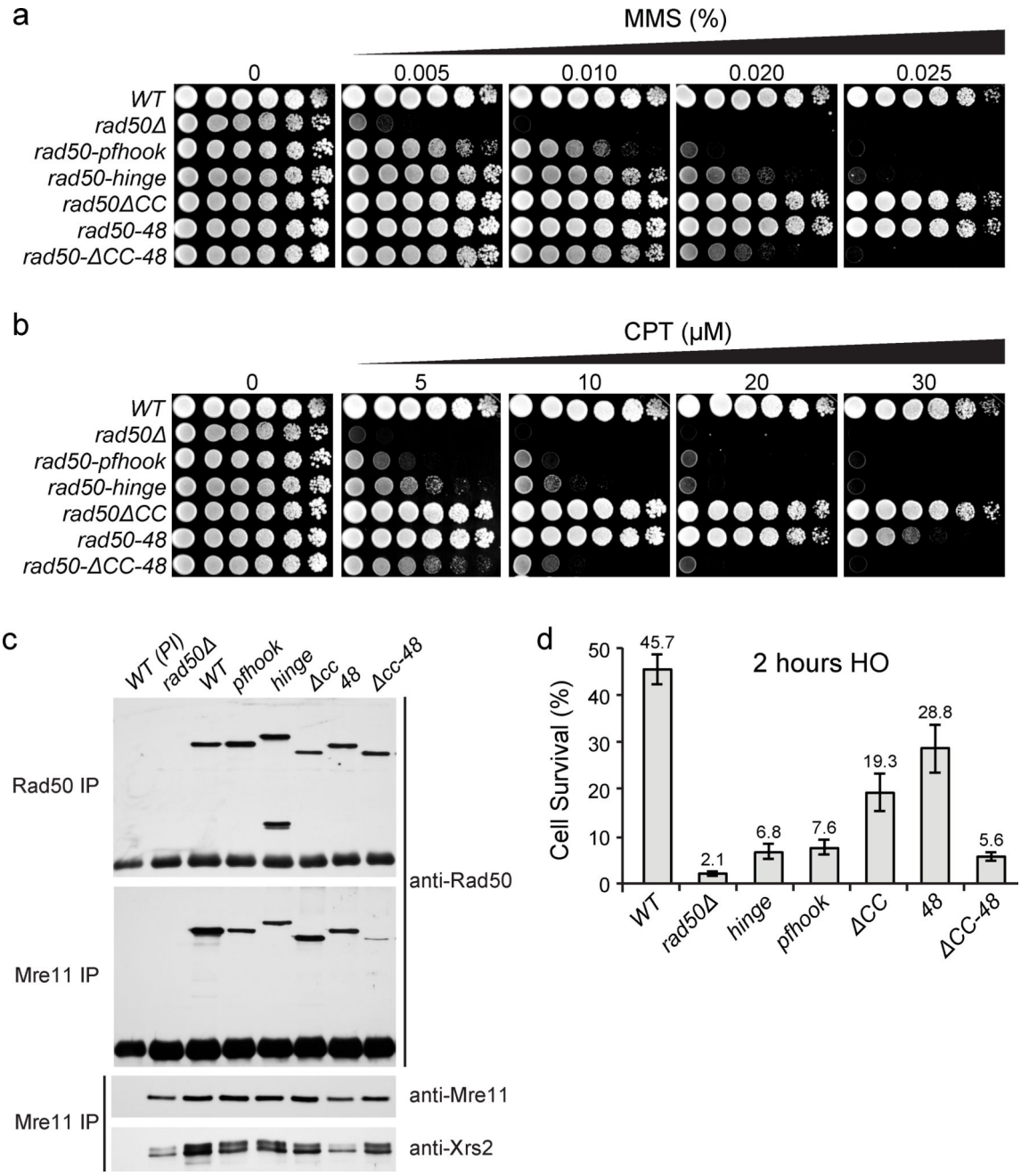

Figure 5. DSB repair and Mre11 complex integrity of Rad50 coiled coil and hook dimerization interface mutants

(a,b) DNA damage sensitivities of the mutants towards clastogens, (a) MMS and (b) CPT. (c) Mre11 complex integrity in wild type (*WT*) and *rad50* "hook" and "coiled-coil" mutants assessed by co-immunoprecipitation and Western blot with Rad50 or Mre11 antisera. Preimmune antibodies (PI) were included as negative controls. (d) Cell survival after acute (2 hr) HO-DSB induction at the *MAT* locus. Graph shows the mean +/− s.d. from three independent experiments. Source data for graphs are available online.

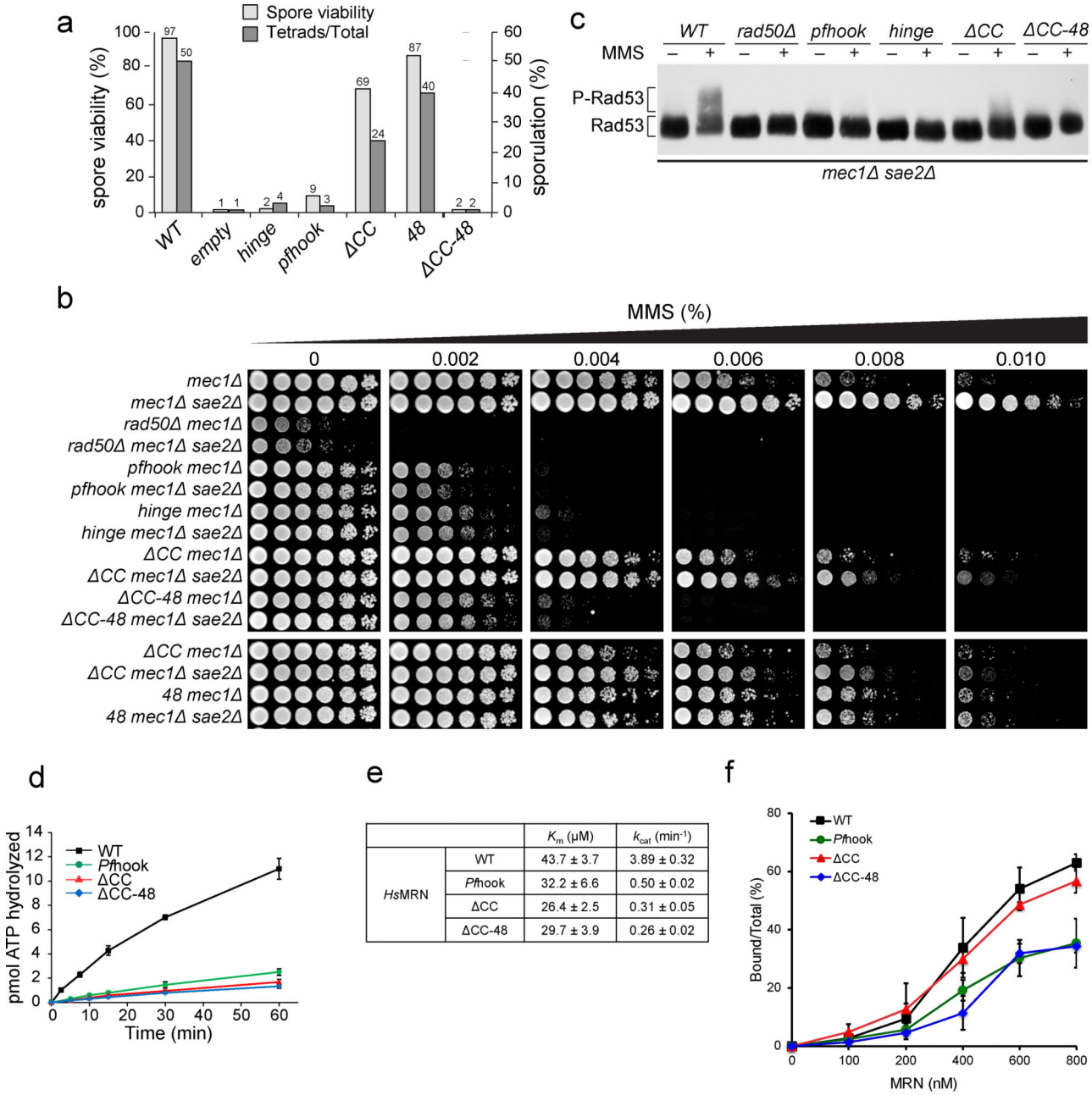

		K_m (μM)	k_{cat} (min^{-1})
*Hs*MRN	WT	43.7 ± 3.7	3.89 ± 0.32
	*Pf*hook	32.2 ± 6.6	0.50 ± 0.02
	ΔCC	26.4 ± 2.5	0.31 ± 0.05
	ΔCC-48	29.7 ± 3.9	0.26 ± 0.02

Figure 6. Effect of Rad50 coiled coil and hook interface mutants on Mre11 complex role in Tel1/ATM checkpoint signaling, meiosis and associated biochemical activities

(a) Spore viability (light gray) and sporulation efficiency (dark gray) of the indicated genotypes were assessed in diploid cells after 48 hr sporulation. Spore viability was determined by tetrad dissection of at least 27 tetrads (% spore viability, y axis on the left). The sporulation efficiency was calculated as the percentage of asci among total number of cells (% tetrads) and graphically illustrated (% sporulation, y axis on the right). Source data for graphs are available online. (b) Cell survival of *rad50*-hook and coiled coil mutants in *mec1Δ* and *mec1Δ sae2Δ* background. All strains also contain the *sml1Δ* mutation. (c) Tel1-dependent Rad53 phosphorylation in Mec1-deficient cells upon MMS treatment (+) assessed

by anti-FLAG-Rad53 Western blot. The migration levels of the nonphosphorylated form (Rad53) and phosphorylated form (P-Rad53) are indicated. (d) ATPase activities of various *Hs*MRN proteins at a substrate concentration of 12.5 uM; Wild-type *Hs*MRN (black square), *Hs*MR(*Pf*hook)N (green circle), *Hs*MR(ΔCC)N (red triangle), and *Hs*MR(ΔCC-48)N (blue diamond) are shown. Graph shows the mean +/− s.d. from three independent experiments. Source data for graphs are available online. (e) Kinetic parameters for the ATP binding and hydrolysis of various *Hs*Mre11 complexes. (f) DNA binding activities of Rad50 WT and mutant *Hs*MRN complexes. Various concentrations of *Hs*MRN complex were incubated in binding buffer in the presence of AMPPNP. WT and mutant complexes are denoted by the same symbols as in Fig. 6d. Bound versus total DNA was quantified in three experiments and the mean +/− s.d is shown in the graph. Representative gel pictures are shown in Supplementary Fig. 5b–e. Source data for graphs are available online.

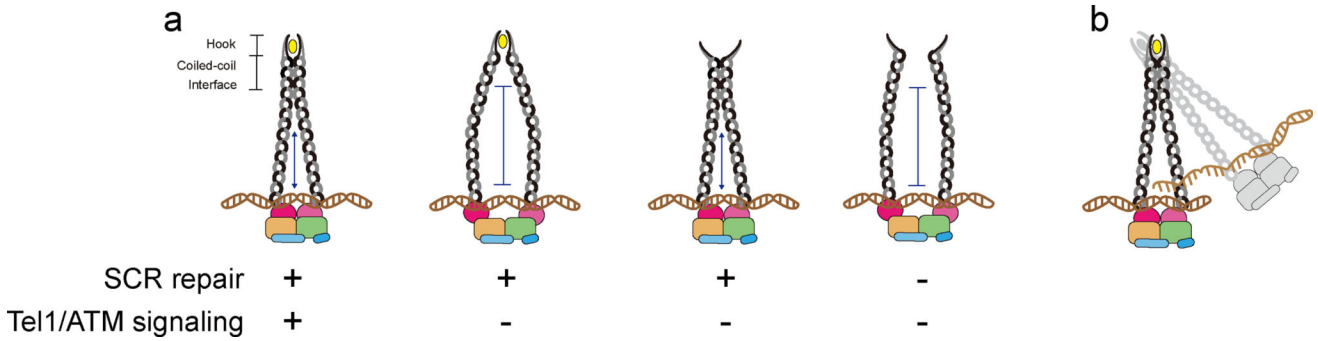

Figure 7. The Rad50 rod-shaped coiled-coil structure at the apex is important for Mre11 complex globular domain functions

(a) From left, rod-shaped intra-complex with intact hook and coiled-coil interfaces orient Mre11 complex globular domain to promote Tel1/ATM signaling and DNA repair by SCR; 2nd and 3rd, The Mre11 complex with disrupted Rad50 coiled-coil interface (or impaired Rad50 hook) retains SCR but is deficient in Tel1/ATM signaling; right, perturbation of both interfaces at the apex may limit the conformational change of the globular domain and disrupt both Tel1/ATM signaling and SCR activity. (b) Oligomerization *via* inter-coiled-coils interaction may facilitate SCR.

Table 1

Data collection and refinement statistics

	*Hs*Rad50HCC182
Data collection	
Space group	$P2_1$
Cell dimensions	
a, *b*, *c* (Å)	42.2, 62.0, 81.5
α, *β*, *γ* (°)	90.0, 99.8, 90.0
	Peak
Wavelength	0.9766
Resolution (Å)	50–2.4 (2.44–2.4)
*R_{merge}	9.4 (71.3)
$I / \sigma I$	42.2 (2.6)
Completeness (%)	99.6 (97)
Redundancy	3.6
Refinement	
Resolution (Å)	30–2.4
No. reflections	16117
¶R_{work} / R_{free}	21.1/27.0
No. atoms	
Protein	2952
Ligand/ion	18/1
Water	9
B factors	
Protein	93.76
Ligand/ion	111.3/100.8
Water	75.4
**r.m.s deviations	
Bond lengths (Å)	0.009
Bond angles (°)	1.302

*Values in parentheses are for the highest shell.

¶$R = \Sigma \mid F_{obs} - F_{calc} \mid / \Sigma F_{obs}$, *where* $F_{obs} = F_{pi}$ and F_{calc} is the calculated protein structure factor from the atomic model (R_{free} was calculated with 5% of the reflections).

**r.m.s. deviation in bond lengths and angles are the deviations from ideal values.